Automated and Network Structure Preserving Segmentation of Optical Coherence Tomography Angiograms

Ylenia Giarratano, Eleonora Bianchi, Calum Gray, Andrew Morris, Tom MacGillivray, Baljean Dhillon and Miguel O. Bernabeu

Abstract—**Optical coherence tomography angiography (OCTA) is a novel non-invasive imaging modality for the visualisation of microvasculature *in vivo*. OCTA has encountered broad adoption in retinal research. OCTA potential in the assessment of pathological conditions and the reproducibility of studies relies on the quality of the image analysis. However, automated segmentation of parafoveal OCTA images is still an open problem in the field. In this study, we generate the first open dataset of retinal parafoveal OCTA images with associated ground truth manual segmentations. Furthermore, we establish a standard for OCTA image segmentation by surveying a broad range of state-of-the-art vessel enhancement and binarisation procedures. We provide the most comprehensive comparison of these methods under a unified framework to date. Our results show that, for the set of images considered, the U-Net machine learning (ML) architecture achieves the best performance with a Dice similarity coefficient of 0.89. For applications where manually segmented data is not available to retrain this ML approach, our findings suggest that optimal oriented flux is the best handcrafted filter enhancement method for OCTA images from those considered. Furthermore, we report on the importance of preserving network connectivity in the segmentation to enable vascular network phenotyping. We introduce a new metric for network connectivity evaluations in segmented angiograms and report an accuracy of up to 0.94 in preserving the morphological structure of the network in our segmentations. Finally, we release our data and source code to support standardisation efforts in OCTA image segmentation.**

Index Terms—**Optical coherence tomography angiography, automated segmentation, retinal vasculature, network structure preservation.**

I. INTRODUCTION

A number of studies over the past years have demonstrated that phenotypes of the retinal vasculature represent important biomarkers for early identification of pathological conditions such as diabetic retinopathy [1], cardiovascular disease [2], and neurodegenerative disease [3]. Therefore, information regarding structural and functional changes in the retinal blood vessels can play a crucial role in the diagnosis and monitoring of these diseases.

Optical coherence tomography angiography (OCTA) is a novel non-invasive imaging modality that allows visualisation of the microvasculature *in vivo* across retinal layers. It is based on the principle of repeating multiple OCT B-scans in rapid succession at each location on the retina. Static tissues will remain the same, while tissues containing flowing red blood cells will show intensity variations over time. OCTA can provide angiograms at different retinal depths and, unlike fluorescein angiography, does not require any dye injection, which may carry the risk of adverse reactions [4].

OCTA diagnosis potential has already been established in the context of neurovascular disease, diabetic retinopathy and, more recently, in chronic kidney disease. In [5], microvascular characteristics calculated from OCTA images are compared between Alzheimer's disease patients, mild cognitive impairment (MCI) patients, and cognitive intact controls. Results showed a decrease in vessel density (VD) and perfusion density (PD) of Alzheimer participants compared with the MCI and controls, opening to the possibility that changes in the retinal microvasculature may mirror small vessel disease in the brain, which is currently not possible to image clinically. Multiple studies on diabetic retinopathy have demonstrated that measurements from the foveal avascular zone (FAZ) in OCTA images are discriminant features in diabetic eyes compared to healthy individuals, even before retinopathy develops [6], [7]. Finally, a recent study on renal impairment [8] demonstrated the potential of OCTA to find associations between changes in the retina and chronic kidney disease (CKD). OCTA scans revealed close association between CKD and lower paracentral retinal vascular density in hypertensive patients.

Measurements used in these studies are based on quantifying phenotypes such as vessel density (VD), fractal dimension (FD), and percentage area of nonperfusion (PAN), extracted from binary masks of OCTA images [9], [10]. However, the accuracy of these measurements and their reproducibility relies on the quality of the image segmentation. Since manual segmentation of blood vessels is a time consuming procedure that requires intra and inter-rater repeatability, there is a necessity to establish a fast automated method not affected by individual subjectivity. The development of automated segmentation algorithms for OCTA images is a novel research field and no consensus exists in the literature about the best approaches. For example, in [11], [12] OCTA phenotypes are calculated on

Y. Giarratano, M. O. Bernabeu and A. Morris, are with the Usher Institute, University of Edinburgh, Edinburgh, EH16 4UX, UK. Emails: {ylenia.giarratano, miguel.bernabeu, andrew.morris}@ed.ac.uk

E. Bianchi is with Princess Alexandra Eye Pavilion, NHS Lothian, Edinburgh, EH3 9HA, UK. Email: e.bianchi@nhs.net

C. Gray is with Edinburgh Imaging, University of Edinburgh, Edinburgh, EH16 4TJ, UK. Email: calum.gray@ed.ac.uk

A. Morris is with Health Data Research UK, London, NW1 2BE, UK. Email: andrew.morris@ed.ac.uk

B. Dhillon is with the School of Clinical Sciences, University of Edinburgh, Edinburgh, EH3 9HA, UK. Email: baljean.dhillon@ed.ac.uk

T. MacGillivray is with the Centre for Clinical Brain Sciences, University of Edinburgh, Edinburgh, EH16 4SB, UK. Email: t.j.macgillivray@ed.ac.uk

manually traced vessels. Simple thresholding procedures are used in [9], [13], [14]. Hessian filters followed by thresholding are applied on the original image to enhance vessels structure in [15], [16]. A convolutional deep neural network approach was proposed in [17] and more recently the U-net architecture was adapted to OCTA in [18]. However, how these different approaches compare to each other is not known. Furthermore, it is currently unknown how these methods perform when it comes to preserving network connectivity in the segmentation. This is a key aspect that can enable advanced vascular network phenotyping based on network science approaches (*e.g.* [19], [20]).

In this work, we take advantage of OCTA images from the PREVENT cohort (https://preventdementia.co.uk/), an ongoing prospective study aimed to predict early onset of dementia [21]. We derive and validate the first open dataset of retinal parafoveal OCTA images with associated ground truth manual segmentations. Furthermore, we establish a standard for OCTA image segmentation by surveying a broad range of state-of-the-art vessel enhancement and binarisation procedures. We provide the most comprehensive comparison of these methods under a unified framework to date. Our results show that, for the set of images considered, the U-Net machine learning (ML) architecture achieves the best performance. For applications where manually segmented data is not available to retrain this ML approach, our findings suggest that optimal oriented flux is the best handcrafted filter enhancement method from those considered. Furthermore, we report on the importance of preserving network connectivity in the segmentation to enable vascular network phenotyping. We introduce a new metric for network connectivity evaluations in segmented microvascular angiograms and report excellent accuracy in preserving the morphological structure of the network in our segmentations. Finally, we release our data and source code to support standardisation efforts in OCTA image segmentation.

II. METHODS

A. Data acquisition

Imaging was performed using the commercial RTVue-XR Avanti OCT system (OptoVue, Fremont, CA). Consequent B-scans, each one consisting of $304{\times}304$ A-scans, were generated in $3{\times}3$ mm and $6{\times}6$ mm fields of view centered at the fovea. Maximum decorrelation value is used to generate *en face* angiograms of superficial, deep and choriocapillary layers. In this work, we selected images only of the superficial layer (containing the vasculature enclosed in the internal limiting membrane layer (ILM) and the inner plexiform layer (IPL)) with $3{\times}3$ mm field of view from left and right eyes of 17 participants with and without family history of dementia as part of a prospective study aimed to find early biomarkers of neurodegenerative diseases (PREVENT). For each of those images we extracted five subimages, one from each clinical region of interest (ROI): superior, nasal, inferior, temporal, and foveal (Figure 1A), up to a total of 170 ROIs. Poor quality ROIs were discarded and from the remaining, 55 ROIs from 11 participants were selected and split into training (30 ROIs) and test (25 ROIs) subgroups.

B. Manual segmentation

A number of challenges need to be overcome in OCTA manual segmentation: images suffer from poor contrast, low signal to noise ratio and can contain motion artifacts generated during the scan acquisition. The most common visible artifacts are vertical and horizontal line distortions, as shown in Figure 1B. Furthermore, the fact that images are constructed from the average of a volume means that, in our segmentation, we cannot distinguish vessels going past each other at different depths. In general, bigger vessels appear brighter and easier to trace, however, the smallest capillaries are challenging to segment and therefore are affected to subjective interpretation by any given rater.

Previous OCTA studies have performed manual continuous blood vessel delineation with or without consideration of vessel width ([17] and [18], respectively). Given the sources of uncertainty previously described, this approach may overinterpret vessel connectivity and suffer from reproducibility issues that remain currently unexplored in the literature. Instead, we adopted a more conservative approach and performed pixelwise manual segmentation (using the ITK-SNAP software [22]). A previous study performing pixelwise segmentation [23] did not assess reproducibility of the segmentations and could not resolve the finest capillaries in the scans.

C. Automated image segmentation methods

Vessel enhancement approaches consist of filters that improve the contrast between vessels and background. We chose four well-known handcrafted filters for blood vessel segmentation, based on implementation availability and previous applications to the enhancement of tubular-like structures in retinal images: *Frangi* [24], *Gabor* [25], *SCIRD-TS* [26], and *OOF* [27]. All these filters require parameter tuning. In our case, from a range of possible configurations we selected the optimal set of parameters that gave the best performance when compared to the manual segmentation (see Supplementary Table S1).

Although handcrafted filters work in many cases, often real images do not satisfy their assumptions (*e.g.* locally tubular structure and gaussian intensity profile). To overcome this issue probabilistic and machine learning frameworks have been proposed [23], [17]. In this study, we considered the latter by implementing two deep learning architectures. We implemented a pixelwise convolutional neural network (CNN) and the more recently proposed U-Net architecture [28]. The design of the CNN for pixelwise classification is based on the one proposed in [17] for OCTA segmentation. It consists of three convolutional layers with rectified linear unit activation (ReLU), each followed by maxpooling. To reduce the risk of overfitting, dropout is used before the last fully connected layer. For each training image we extracted the same number of vessel and background pixels to balance the classes. A patch containing the pixel to classify and its 61×61 neighbourhood is used as input to the network. More than 200,000 patches were used during the training. Finally, the probability of belonging to a vessel or background is then used to generate the enhanced grayscale image (see Supplementary Table S2).
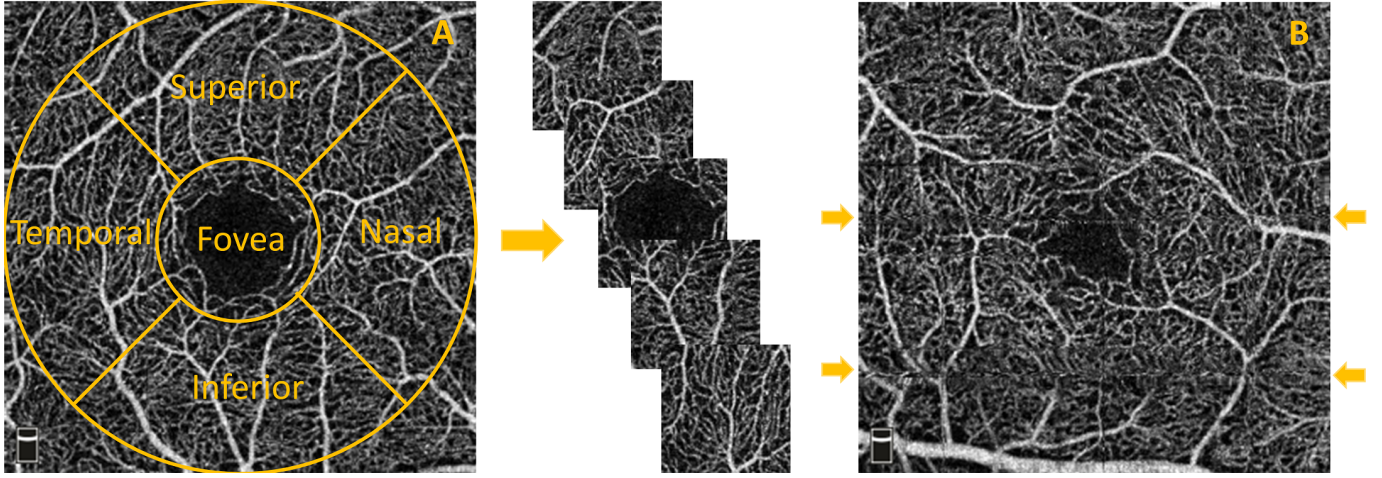
Fig. 1. (A) Extraction of images from each clinical region of interest: superior, nasal, foveal, inferior, and temporal. (B) Examples (arrows) of horizontal artifacts in OCTA images.

Developed for biomedical image segmentation, U-Net is a fully convolutional neural network characterised by a contracting path and an expansive path that confer to the network its U shape. It has proved to be fast and accurate even with few training images. The architecture consists of modules of two repeated convolutional layers with ReLU activation function followed by maxpooling for the encoder path, upsampling and two repeated convolutional layers for the decoder path (see Supplementary Table S3). The lowest resolution is 8×8 pixels and binary cross entropy is used as loss function. From each ROI, 1,000 patches of size 32×32 are extracted to train the network, for a total of 30,000 training inputs. Given our initial sample size, data augmentation (flipping horizontally or vertically) has been used in both CNN and U-Net.

Vessel enhancement is often followed by a threshold step to obtain the vessel binary mask. However, modern methods employ the enhanced vasculature as a preliminary step for more advanced binarisation algorithms, such as machine learning (ML) classifiers. Therefore, we decided to compare adaptive thresholding, which is a form of thresholding that takes into account spatial variations in illumination, with support vector machines (SVMs), random forest (RF) and k-nearest neighbours (k-NN) as binarisation procedure in the case of Frangi, Gabor, SCIRD-TS. A two step binarisation procedure, suggested in [29] has been used in the case of OOF. Finally, a global thresholding is used to binarise the probability maps obtained from the CNN architecture, based on the shape of the pixel intensity histogram, and adaptive thresholding on the one obtained from the U-Net. In each of the ML binary classifiers we used seven features to characterise pixels: intensity based features extracted from a 3×3 pixel neighbourhood (intensity value, range, average, standard deviation, and entropy) and geometric features (the local curvature information provided by the hessian eigenvalues), [30].

D. Segmentation evaluation

Cohen's kappa coefficient is a robust statistic for testing intra and inter-rater variability. Considering $Pr(a)$ and $Pr(e)$

as the observed agreement and the chance agreement, respectively, it can be computed as:

$$\kappa = \frac{Pr(a) - Pr(e)}{1 - Pr(e)}. \tag{1}$$

In our study $Pr(a)$ is the accuracy in pixel classification (vessel *vs* background) and $Pr(e)$ is the sum of the probability of both raters randomly selecting vessel pixels and the probability of both of them randomly selecting background pixels for a given ROI.

For the ROIs in the test set, pixelwise comparison between manual and automated segmentation was performed using Dice similarity coefficient defined as

$$Dice = \frac{2TP}{2TP + FP + FN}, \tag{2}$$

where TP, FP, FN represent true positive, false positive and false negative, respectively.

Furthermore, for the evaluation of the agreement in network morphology between manual and automated segmentations, we used the CAL metric proposed in [31]. It is based on three descriptive features:

- connectivity (C), to assess the fragmentation degree between segmentations, described mathematically by the formula

$$C(S, S_{GT}) = 1 - min\left(1, \frac{|\#_C S_{GT} - \#_C S|}{\#S_{GT}}\right) \tag{3}$$

where $\#_C S$ and $\#_C S_{GT}$ are the number of connected components in the segmented and ground truth image, while $\#S_{GT}$ is the number of vessel pixels in the mask;

- area (A), to evaluate the degree of overlapping, defined as

$$A(S, S_{GT}) = \frac{\#((\delta_\alpha(S) \cap S_{GT}) \cup (S \cap \delta_\alpha(S_{GT}))}{\#(S \cup S_{GT})}, \tag{4}$$

where δ_α is a morphological dilatation using a disc of radius α;

- length (L), to capture the degree of coincidence, described by

$$L(S, S_{GT}) = \frac{\#((\varphi(S) \cap \delta_\beta S_{GT})) \cup (\delta_\beta(S) \cap \varphi(S_{GT}))}{\#(\varphi(S) \cup \varphi(S_{GT}))},$$ (5)

where φ indicates a skeletonisation procedure and δ_β is a morphological dilatation using a disc of radius β.

In this study we set α and β both equal to 1. The product of C, A, and L, (CAL) results sensitive to the vascular features and takes values in the range [0,1], with the zero denoting the worst segmentation and 1 the perfect segmentation.

Finally, since we are interested in penalising methods that introduce disconnections in the segmentation of the largest connected component of the network, we introduce a new metric, namely the largest connected component ratio (LCC), defined as:

$$LCC = 1 - \frac{|\#LCC_S - \#LCC_{GT}|}{\#LCC_{GT}},$$ (6)

where $\#LCC_S$ and $\#LCC_{GT}$ are the lengths, in terms of number of pixels, of the largest connected component in the skeleton of the segmented and ground truth images. The closest to 1 is the LCC ratio, the more similar is in structure the largest connected component of the segmented image compared to the ground truth.

III. RESULTS

A. Inter and intra-rater agreements

The ground truth dataset contains 55 ROIs segmented by one rater (rater A). Rater A (Y.G.) segmented 20 images twice, and rater B (E.B.) performed the same task on another 20 images once. We calculated the Cohen's kappa coefficient for each pairwise comparison. Results show good agreements (for each pair $k > 0.7$) with an average of 0.8 for the intra rater agreement and 0.77 between operators, which demonstrates that the proposed approach to segmentation is reproducible.

B. Automated approaches for pixelwise classification

Segmentation performances are shown in Table I. The U-Net outperforms all the other methods, by reaching a Dice score of 0.89. Among the handcrafted filters, OOF and Frangi filters achieve good performances with an average Dice score of 0.86 and 0.85, respectively. The use of machine learning methods as binarisation procedure slightly improve performances compared to the thresholding procedure in Frangi, Gabor and SCIRD-TS. Investigating the enhanced images (Figure 2), we noticed that each method suffers from different deficiencies. Frangi filter clusters nearby vessels, losing important information contained in the microvasculature. Gabor filter enhances centrelines, performing poorly on the detection of vessel edges. SCIRD-TS remodels the vasculature making it more regular and equally spaced. OOF retrieves the smallest capillaries but overenhances noise in the foveal region. Figure 3 shows segmentation results after applying each vessel enhancement method and best binarisation procedure. Figure 4 shows whole image segmentations with the best handcrafted and learnt filters.

TABLE I
TABLE OF PERFORMANCES IN TERMS OF DICE SIMILARITY COEFFICIENT, CAL AND LCC RATIO.

	Performance measure		
Method	**Dice**	**CAL**	**LCC ratio**
Frangi+Threshing	0.83	0.83	0.88
Frangi+k-NN	0.84	0.86	0.91
Frangi+SVM	0.85	0.87	0.94
Frangi+RF	0.85	0.87	0.94
Method	**Dice**	**CAL**	**LCC ratio**
Gabor+Threshing	0.77	0.75	0.76
Gabor+k-NN	0.82	0.84	0.83
Gabor+SVM	0.83	0.85	0.84
Gabor+RF	0.83	0.85	0.87
Method	**Dice**	**CAL**	**LCC ratio**
SCIRD-TS+Threshing	0.71	0.66	0.68
SCIRD-TS+k-NN	0.72	0.74	0.90
SCIRD-TS+SVM	0.75	0.75	0.75
SCIRD-TS+RF	0.74	0.75	0.80
Method	**Dice**	**CAL**	**LCC ratio**
OOF	**0.86**	**0.85**	**0.94**
CNN	0.83	0.85	0.94
U-Net	**0.89**	**0.89**	**0.93**

C. Foveal avascular zone

Foveal images are characterised by the presence of a predominant dark area called foveal avascular zone (FAZ), due to the fact that it is free from blood vessels. We noticed that handcrafted filters have difficulties with those images, overenhancing noise in the central region (Figure 5). This led to vessel detection in the FAZ when thresholding methods are applied. Machine learning methods were less affected by this issue since they learnt from the ground truth data. These results demonstrate the necessity for more investigations towards preprocessing procedures that can reduce the noise in the FAZ without affecting the properties of the vascular network when handcrafted filters are used for vessel enhancement.

IV. DISCUSSION AND CONCLUSIONS

Retinal image analysis has demonstrated great potential for the discovery of biomarkers of eye and systemic disease. Recently, OCTA imaging has enabled the visualisation of the smallest capillaries in the retina without the need of a contrast agent. However, its potential for the assessment of pathological conditions and the reproducibility of studies based on it rely on the quality of the image analysis. Automated OCTA image segmentation is an open problem in the field. In this study, we generate the first open dataset of retinal parafoveal OCTA images with associated ground truth manual segmentations. We pay special attention to segmenting the images in a reproducible way and demonstrate good inter- and intra-rater agreement. Furthermore, we establish a standard for automated OCTA image segmentation by surveying a broad
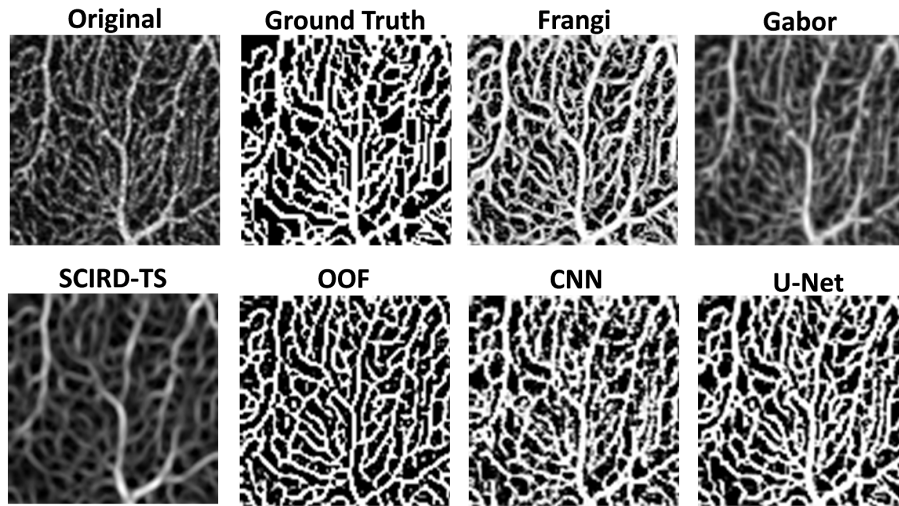
Fig. 2. Example of vessels enhancement. Original, ground truth and images after vessel enhancement by using Frangi, Gabor, SCIRD-TS, OOF, CNN, and U-Net.
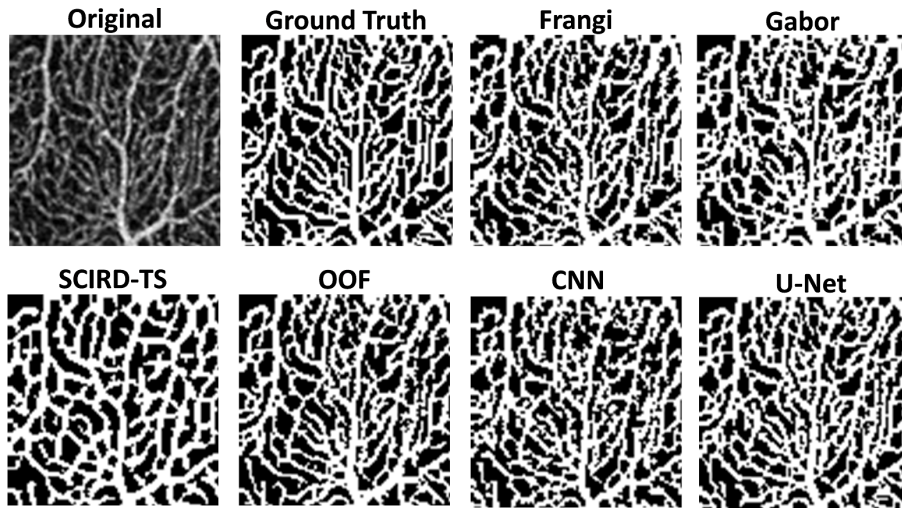

Fig. 3. Vessel segmentation in superior parafoveal OCTA image. Original, ground truth images followed by binary images after vessel enhancement by using Frangi (+RF), Gabor (+RF), SCIRD-TS (+SVM), OOF, CNN, and U-Net.
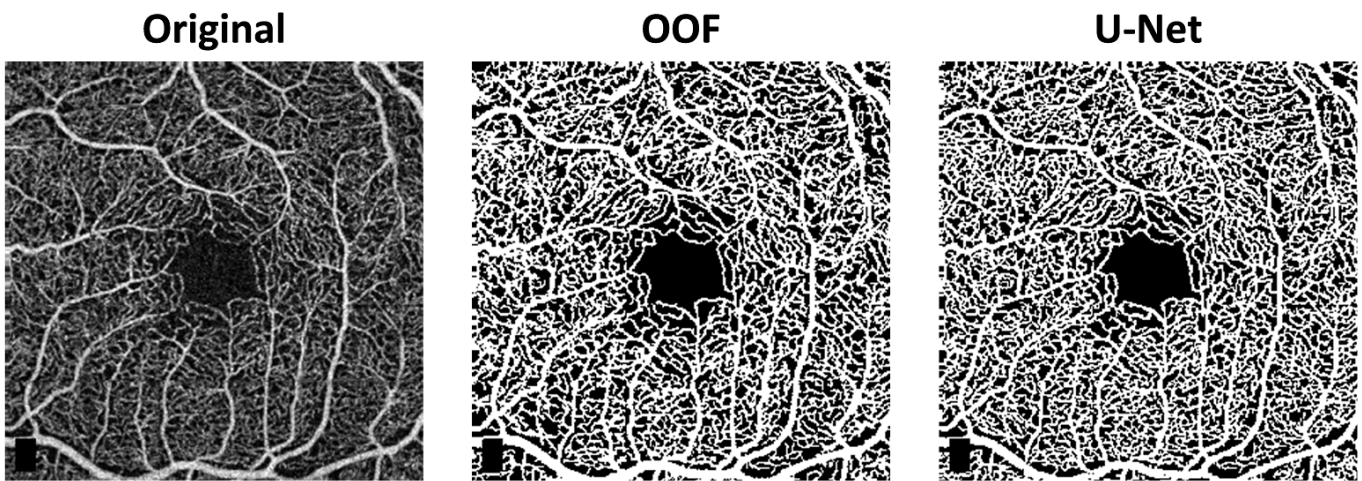

Fig. 4. Whole image segmentation by using the best two methods, OOF and U-Net. Optovue RTVue XR Avanti scan logo on the bottom left corner was removed from the original image.
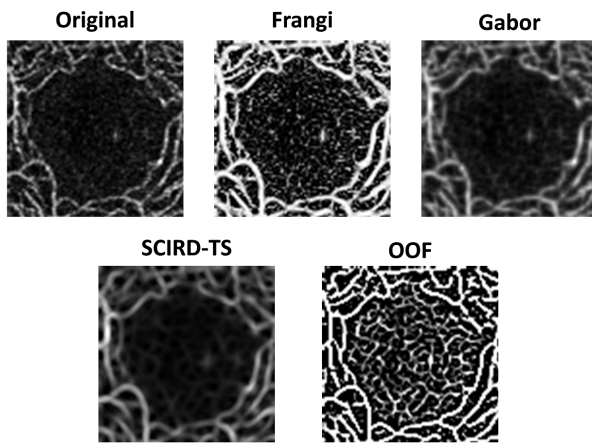
Fig. 5. Foveal images: exxamples of enhancement in the FAZ.

range of openly available state-of-the-art vessel enhancement and binarisation procedures. We present a comparison of these methods under a unified computational framework and make the source code available. We evaluate segmentation quality measures to guide the identification of the algorithm that not only provides the best agreement with the manually segmented images, but also achieves the best preservation of their network morphology. We believe that this will open the door to the development of novel vascular morphology metrics based on the application of network science principles capable of deeply phenotyping retinal vasculature.

Our results indicate that, for the set of images considered, the U-Net architecture is the best automated segmentation method for parafoveal OCTA images, since it achieves the best performances in Dice similarity coefficient. Our U-Net implementation achieves better results than the one presented in [18] and comparable to the best results reported to date [23]. However, like-for-like comparison of methods across the literature is difficulted by a lack of consistency in the approach to manual segmentation (*e.g.* ability to resolve finest capillaries in the OCTA images [23] and consideration of vessel width in the segmentations [18]). Our study provides the necessary tools to standardise method comparison in the future. Interestingly, OOF achieves segmentation performances in line with the neural network architectures without the requirement of extensive manually segmented images for training purposes. We found that in our analysis, ML techniques improved segmentation performance when used as binarisation methods following handcrafted filter enhancement. Furthermore, we report on the importance of preserving network connectivity in the segmentation to enable vascular network phenotyping. We introduce a new metric for network connectivity evaluations in segmented angiograms, to be used in conjunction with pixelwise similarity coefficients such as Dice, and report excellent accuracy in preserving the morphological structure of the network in our segmentations.

Our results highlight challenges in the segmentation of the FAZ: handcrafted filters suffer from noise enhancement in this region, indicating the necessity of masking that area or the use of more sophisticated denoising preprocessing procedures

when those filters are applied. Future work will involve the characterisation of FAZ signal as either noise or signal from deeper layers and research towards improved network structure preserving segmentation algorithms, *e.g.* improving the connectivity in the U-Net segmentation including topological information into the loss function of the learning process [32].

REFERENCES

[1] A. J. Jenkins, M. V. Joglekar, A. A. Hardikar, A. C. Keech, D. N. O'Neal, and A. S. Januszewski, "Biomarkers in diabetic retinopathy," *Review of Diabetic Studies*, vol. 12, no. 1-2, pp. 159–195, 2015.

[2] R. Poplin, A. V. Varadarajan, K. Blumer, Y. Liu, M. V. McConnell, G. S. Corrado, L. Peng, and D. R. Webster, "Prediction of cardiovascular risk factors from retinal fundus photographs via deep learning," *Nature Biomedical Engineering*, vol. 2, no. 3, pp. 158–164, 2018.

[3] D. C. DeBuc, G. M. Somfai, and A. Koller, "Retinal microvascular network alterations: Potential biomarkers of cerebrovascular and neural diseases," *American Journal of Physiology - Heart and Circulatory Physiology*, vol. 312, no. 2, pp. H201–H212, 2017.

[4] F. Musa, W. J. Muen, R. Hancock, and D. Clark, "Adverse effects of fluorescein angiography in hypertensive and elderly patients," *Acta Ophthalmologica Scandinavica*, vol. 84, no. 6, pp. 740–742, 2006.

[5] S. P. Yoon, D. S. Grewal, A. C. Thompson, B. W. Polascik, C. Dunn, J. R. Burke, and S. Fekrat, "Retinal Microvascular and Neurodegenerative Changes in Alzheimer's Disease and Mild Cognitive Impairment Compared with Control Participants," *Ophthalmology Retina*, vol. 3, no. 6, pp. 489–499, 2019. [Online]. Available: https://doi.org/10.1016/j.oret.2019.02.002

[6] J. Khadamy, K. Aghdam, and K. Falavarjani, "An update on optical coherence tomography angiography in diabetic retinopathy," *Journal of Ophthalmic & Vision Research*, vol. 13, p. 487, 10 2018.

[7] N. Takase, M. Nozaki, A. Kato, H. Ozeki, M. Yoshida, and Y. Ogura, "Enlargement of foveal avascular zone in diabetic eyes evaluated by en face optical coherence tomography angiography," *Retina*, vol. 35, no. 11, pp. 2377–2383, 2015.

[8] M. Vadalà, M. Castellucci, G. Guarrasi, M. Terrasi, T. La Blasca, and G. Mulè, "Retinal and choroidal vasculature changes associated with chronic kidney disease," *Graefe's Archive for Clinical and Experimental Ophthalmology*, vol. 257, no. 8, pp. 1687–1698, 2019.

[9] P. L. Nesper, P. K. Roberts, A. C. Onishi, H. Chai, L. Liu, L. M. Jampol, and A. A. Fawzi, "Quantifying Microvascular Abnormalities With Increasing Severity of Diabetic Retinopathy Using Optical Coherence Tomography Angiography," *Investigative ophthalmology & visual science*, vol. 58, no. 6, pp. BIO307–BIO315, 2017.

[10] R. Reif, J. Qin, L. An, Z. Zhi, S. Dziennis, and R. Wang, "Quantifying optical microangiography images obtained from a spectral domain optical coherence tomography system," *International Journal of Biomedical Imaging*, vol. 2012, 2012.

[11] A. Y. Alibhai, E. M. Moult, R. Shahzad, C. B. Rebhun, C. Moreira-neto, M. Mcgowan, D. Lee, B. Lee, C. R. Baumal, A. J. Witkin, E. Reichel, J. S. Duker, J. G. Fujimoto, and N. K. Waheed, "HHS Public Access," vol. 2, no. 5, pp. 418–427, 2019.

[12] B. D. Krawitz, S. Mo, L. S. Geyman, S. A. Agemy, N. K. Scripsema, P. M. Garcia, T. Y. Chui, and R. B. Rosen, "Acircularity index and axis ratio of the foveal avascular zone in diabetic eyes and healthy controls measured by optical coherence tomography angiography," *Vision Research*, vol. 139, pp. 177–186, 2017.

[13] A. C. Onishi, P. L. Nesper, P. K. Roberts, G. A. Moharram, H. Chai, L. Liu, L. M. Jampol, and A. A. Fawzi, "Importance of considering the middle capillary plexus on OCT angiography in diabetic retinopathy," *Investigative Ophthalmology and Visual Science*, vol. 59, no. 5, pp. 2167–2176, 2018.

[14] T. S. Hwang, S. S. Gao, L. Liu, A. K. Lauer, C. J. Flaxel, D. J. Wilson, D. Huang, Y. Jia, and O. Health, "HHS Public Access," vol. 134, no. 4, pp. 367–373, 2016.

[15] A. Y. Kim, Z. Chu, A. Shahidzadeh, R. K. Wang, C. A. Puliafito, and A. H. Kashani, "Quantifying microvascular density and morphology in diabetic retinopathy using spectral-domain optical coherence tomography angiography," *Investigative Ophthalmology and Visual Science*, vol. 57, no. 9, pp. OCT362–OCT370, 2016.

[16] M. Zhang, T. S. Hwang, C. Dongye, D. J. Wilson, D. Huang, and Y. Jia, "Automated quantification of nonperfusion in three retinal plexuses using projection-resolved optical coherence tomography angiography in diabetic retinopathy," *Investigative Ophthalmology and Visual Science*, vol. 57, no. 13, pp. 5101–5106, 2016.

[17] P. Prentašic, M. Heisler, Z. Mammo, S. Lee, A. Merkur, E. Navajas, M. F. Beg, M. Šarunic, and S. Loncaric, "Segmentation of the foveal microvasculature using deep learning networks," *Journal of Biomedical Optics*, vol. 21, no. 7, p. 075008, 2016.

[18] L. Mou, Y. Zhao, L. Chen, J. Cheng, Z. Gu, H. Hao, H. Qi, Y. Zheng, A. Frangi, and J. Liu, *CS-Net: Channel and Spatial Attention Network for Curvilinear Structure Segmentation*, 10 2019, pp. 721–730.

[19] I. Amat-Roldan, A. Berzigotti, R. Gilabert, and J. Bosch, "Assessment of hepatic vascular network connectivity with automated graph analysis of dynamic contrast-enhanced us to evaluate portal hypertension in patients with cirrhosis: A pilot study1," *Radiology*, vol. 277, no. 1, pp. 268–276, 2015.

[20] A. P. Alves, O. N. Mesquita, J. Gómez-Gardeñes, and U. Agero, "Graph analysis of cell clusters forming vascular networks," *Royal Society Open Science*, vol. 5, no. 3, 2018.

[21] C. W. Ritchie, K. Wells, and K. Ritchie, "The PREVENT research programme-A novel research programme to identify and manage midlife risk for dementia: The conceptual framework," *International Review of Psychiatry*, vol. 25, no. 6, pp. 748–754, 2013.

[22] P. A. Yushkevich, J. Piven, H. Cody Hazlett, R. Gimpel Smith, S. Ho, J. C. Gee, and G. Gerig, "User-guided 3D active contour segmentation of anatomical structures: Significantly improved efficiency and reliability," *Neuroimage*, vol. 31, no. 3, pp. 1116–1128, 2006.

[23] N. Eladawi, M. Elmogy, O. Helmy, A. Aboelfetouh, A. Riad, H. Sandhu, S. Schaal, and A. El-Baz, "Automatic blood vessels segmentation based on different retinal maps from OCTA scans," *Computers in Biology and Medicine*, vol. 89, no. August, pp. 150–161, 2017.

[24] A. F. Frangi, W. J. Niessen, K. L. Vincken, and M. A. Viergever, "Multiscale vessel enhancement filtering," in *Medical Image Computing and Computer-Assisted Intervention - MICCAI'98*, ser. Lecture Notes in Computer Science, A. C. W.M. Wells and S. Delp, Eds., vol. 1496. Berlin, Germany: Springer Verlag, 1998, pp. 130–137.

[25] J. V. Soares, J. J. Leandro, R. M. Cesar, H. F. Jelinek, and M. J. Cree, "Retinal vessel segmentation using the 2-D Gabor wavelet and supervised classification," *IEEE Transactions on Medical Imaging*, vol. 25, no. 9, pp. 1214–1222, 2006.

[26] R. Annunziata and E. Trucco, "Accelerating Convolutional Sparse Coding for Curvilinear Structures Segmentation by Refining SCIRD-TS Filter Banks," *IEEE Transactions on Medical Imaging*, vol. 35, no. 11, pp. 2381–2392, 2016.

[27] M. W. Law and A. C. Chung, "Three dimensional curvilinear structure detection using optimally oriented flux," in *Computer Vision - ECCV 2008*, vol. 5305. Springer, 2008, pp. 368–382.

[28] O. Ronneberger, P. Fischer, and T. Brox, "U-net: Convolutional networks for biomedical image segmentation," in *Medical Image Computing and Computer-Assisted Intervention – MICCAI 2015*, N. Navab, J. Horneg-

ger, W. M. Wells, and A. F. Frangi, Eds. Cham: Springer International Publishing, 2015, pp. 234–241.

[29] A. Li, J. You, C. Du, and Y. Pan, "Automated segmentation and quantification of OCT angiography for tracking angiogenesis progression," *Biomedical Optics Express*, vol. 8, no. 12, p. 5604, 2017.

[30] P. Rodrigues, P. Guimarães, T. Santos, S. Simão, T. Miranda, P. Serranho, and R. Bernardes, "Two-dimensional segmentation of the retinal vascular network from optical coherence tomography," *Journal of Biomedical Optics*, vol. 18, no. 12, p. 126011, 2013.

[31] M. E. Gegundez-Arias, A. Aquino, J. M. Bravo, and D. Marin, "A function for quality evaluation of retinal vessel segmentations," *IEEE Transactions on Medical Imaging*, vol. 31, no. 2, pp. 231–239, 2012.

[32] J. R. Clough, I. Oksuz, N. Byrne, J. A. Schnabel, and A. P. King, "Explicit Topological Priors for Deep-Learning Based Image Segmentation Using Persistent Homology," *Lecture Notes in Computer Science*, vol. 11492 LNCS, no. 40119, pp. 16–28, 2019.

Appendix

Supplementary material

TABLE S1
TABLE OF PARAMETERS FOR THE HANDCRAFTED FILTERS

	Parameters	
Frangi	FrangiScaleRange	[0.5, 2]
	FrangiScaleRatio	0.5
	FrangiBetaOne	1
	FrangiBetaTwo	15
Gabor	scales	[1,2,3,4]
	epsilon	4
	k0	[0 3]
SCIRD–TS	$fb\_parameters.sigma\_1$	[1,5]
	$fb\_parameters.sigma\_1\_step$	0.5
	$fb\_parameters.sigma\_2$	[1,2]
	$fb\_parameters.sigma\_2\_step$	0.5
	$fb\_parameters.k$	[-0.1, 0.1]
	$fb\_parameters.k\_step$	0.025
	$fb\_parameters.angle\_step$	10
	$fb\_parameters.filter\_size$	9
	$alpha$	0.05
OOF	range	[0.5, 2]
	sigma	0.5
	upthreshold	70

TABLE S2
CNN LAYERS ARCHITECTURE

Layer	Type	Maps and size	Kernel size
0	Input	1 map of 61×61 neurons	
1	Convolution2D	32 maps of 56×56 neurons	6×6
2	Maxpooling2D	32 maps of 28×28 neurons	2×2
3	Convolution2D	32 maps of 24×24 neurons	5×5
4	Maxpooling2D	32 maps of 12×12 neurons	2×2
5	Convolution2D	32 maps of 9×9 neurons	4×4
6	Maxpooling2D	32 maps of 5×5 neurons	2×2
7	Dense	150 neurons	
8	Dropout		
9	Dense	1 neuron	

TABLE S3
U-NET LAYERS ARCHITECTURE

Layer	Type	Maps and size	Kernel size
0	Input	1 map of 32×32 neurons	
1	Convolution2D	32 maps of 32×32 neurons	3×3
2	Convolution2D	32 maps of 32×32 neurons	3×3
3	Maxpooling2D	32 maps of 16×16 neurons	2×2
4	Convolution2D	64 maps of 16×16 neurons	3×3
5	Convolution2D	64 maps of 16×16 neurons	3×3
6	Maxpooling2D	64 maps of 8×8 neurons	2×2
7	Convolution2D	128 maps of 8×8 neurons	3×3
8	Convolution2D	128 maps of 8×8 neurons	3×3
9	Upsampling2D	128 maps of 16×16 neurons	2×2
10	Concatenate	192 maps of 16×16 neurons	
11	Convolution2D	64 maps of 16×16 neurons	3×3
12	Convolution2D	64 maps of 16×16 neurons	3×3
9	Upsampling2D	64 maps of 32×32 neurons	2×2
10	Concatenate	96 maps of 32×32 neurons	
11	Convolution2D	32 maps of 32×32 neurons	3×3
12	Convolution2D	32 maps of 32×32 neurons	3×3
13	Convolution2D	1 map of 32×32 neurons	3×3